Rojas, Felix and Kennel, Ralph and Cardenas, Roberto and Clare, Jon C. and Diaz, Matias (2016) A new space-vector-modulation algorithm for a three-level four-leg NPC inverter. IEEE Transactions on Energy Conversion, PP (99). pp. 1-13. ISSN 0885-8969

Access from the University of Nottingham repository:

http://eprints.nottingham.ac.uk/37541/1/A%20new%20space-vector-modulation%20algorithm%20for%20a%20three-level%20four-leg%20NPC%20inverter.pdf

A New Space-Vector-Modulation Algorithm for a Three-Level Four-Leg NPC Inverter

Felix Rojas, Ralph Kennel, *IEEE Senior Member,* Roberto Cardenas, *IEEE Senior Member,*
Ricardo Repenning, *IEEE Member,* Jon Clare, *IEEE Senior Member,* and Matias Diaz, *IEEE Student Member*

Abstract—**For power conversion systems interfaced to 4-wire supplies, four-leg converters have become a standard solution. A four-leg converter allows good compensation of zero-sequence harmonics and full utilization of the dc-link voltage. These are very important features when unbalanced and/or non-linear loads are connected to the system. This paper proposes a 3D-SVM algorithm and provides a comprehensive analysis of the algorithm implemented on a three-level, four-leg NPC converter. The algorithm allows a simple definition of the different switching patterns and enables balancing of the dc-link capacitor voltages using the redundancies of the converter states. A resonant controller is selected as the control strategy to validate the proposed SVM algorithm in a 6kW experimental rig.**

Index Terms—**Four-Leg Converters, Three level Neutral Point Clamped (NPC) inverter, Three Dimensional Space Vector Modulation (3D-SVM).**

I. INTRODUCTION

THE Neutral-Point-Clamped (NPC) Voltage-Source Inverter (VSI) is currently the most widely used multilevel converter topology [1], [2], [3]. Three-level NPC inverters have well known advantages over the conventional two-level converter. For instance NPC converters can be connected to medium voltage systems without requiring a power transformer [4], they can operate with a relatively high effective switching frequency reducing the total harmonic distortion at the grid/load [5]. Moreover, for a similar application an NPC inverter requires a smaller power filter when compared with a conventional two-level VSI [5]. In addition, lower *dv/dt* values, higher efficiency and less stress on the devices are also considered important advantages of the NPC converter over the conventional two-level topology [3], [5]. There are several applications of the three-level VSI reported in the literature, for instance in Wind Energy Conversion Systems (WECSs) [4], [6], [7], where the nominal power of single WECs approaches

Felix Rojas is with the Electrical Engineering Department, University of Santiago of Chile, Avenida Ecuador N 3519, Estacion Central, Santiago (email felix.rojas@usach.cl).

Ralph Kennel is with the Institute for Electrical Drive Systems and Power Electronics, Technical University of Munich, Arcisstr. 21, 80333, Munich (email ralph.kennel@tum.de).

Roberto Cardenas and Matias Diaz are with the Electrical Engineering Department, University of Chile, Avenida Tupper 2007, Santiago, Chile (email rcd@ieee.org, mdiaz@ing.uchile.cl).

Jon Clare is with the Department of Electrical and Electronic Engineering, University of Nottingham, Nottingham University Park, Nottingham, NG7, 2RD, (email jon.clare@nottingham.ac.uk).
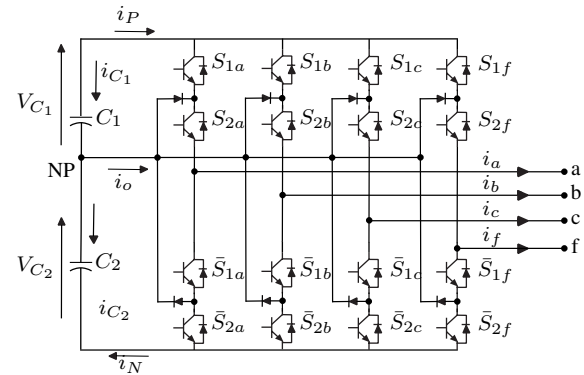

Fig. 1. Electrical diagram for a four-leg Neutral-Point-Clamped Inverter

10MW. In Photovoltaic (PV) applications the three-level NPC is also used because of its good efficiency [1]. Furthermore, applications of the NPC converter as an active filter in medium voltage (MV) systems have been also reported [8].

When a path for the circulation of zero-sequence currents is required, four-leg converters are considered to be one of the solutions offering most advantages [9],[10]. Several topologies of 4-leg converters have been discussed in the literature, for instance applications of the 4-leg, 2-level VSI [11], [12], [9], [13] or 4-leg matrix converter [14], [15] have been extensively studied and can be considered relatively mature technologies. 4-leg multilevel converters, on the other hand, offer higher efficiency, lower switching losses, higher nominal voltage range and lower harmonic distortion. However, they have only been proposed recently as an interesting solution for 4-wire systems, for example in [5], [16], [17] where the application of three-level, 4-leg converters is discussed.

Recent research on control systems and modulation algorithms for four-leg NPC converters have addressed waveform generation and current regulation using non-linear controllers such as Finite-Set Model Predictive Control (FS-MPC), to track output voltage/current references [18], [19]. Unfortunately, variability of the switching frequency and the variable performance at different operating points are potential drawbacks of this approach for grid connected applications. The use of carrier-based Pulse Width Modulation (PWM) applied independently to each leg of the converter has been addressed in [20]. However such strategies do not allow selection of variable vector switching sequences to manipulate the harmonic spectrum or the distribution of the switching power losses, which are important in MV or grid connected applications. A three dimensional modulation approach for 4-leg three-level NPC converters has been proposed in [21],

where the modulation is implemented directly in the *abc* coordinate frame. Although this method is simple, efficient and achieves full utilization of the dc-link voltage, it has some inherent limitations due to the use of the *abc* co-ordinate frame. Firstly, it is complex to analyse/implement overmodulation algorithms in the *abc* frame. On the other hand, using $\alpha\beta\gamma$ coordinates , it is simple to conclude that the outer boundaries of the modulation region are defined only by the dc-link voltage value regardless of the topology and number of levels available in the converter. In addition spacial symmetry issues considerably simplify the implementation of overmodulation strategies in $\alpha\beta\gamma$ coordinates. Moreover over-modulation methods already developed for four-leg converters [22], [23] cannot be applied to algorithms implemented in *abc* coordinates. Secondly, the symmetries of the $\alpha\beta\gamma$ space can be also exploited to allow shaping of the harmonic spectrum of the modulated voltage waveform, e.g. eliminating even-order harmonics from the output signals [24]. This is not achievable in an *abc* frame. Thirdly, the natural decoupling of the zero-sequence component in $\alpha\beta\gamma$ coordinates allows direct control over the zero-sequence, which is very important for four-wire applications. This is difficult to achieve using an *abc* reference frame, where the zero-sequence component is not represented as an independent variable.

This paper proposes, analyses and experimentally validates an SVM algorithm in the $\alpha\beta\gamma$ coordinate frame for a 6kW multilevel NPC four-leg converter. The algorithm has been formulated to consider important features such us: full util-isation of the dc-link voltage, fixed and definable switching frequency, adjustable distribution of power losses among the switches, arrangement of the vectors for implementing dif-ferent switching patterns, utilisation of the redundant vectors for balancing the dc-link voltages under unbalanced or non-linear loads and modulation of unbalanced and non-sinusoidal voltages at the converter outputs.

For all of the aforementioned reasons, we have chosen in this paper to theoretically and experimentally investigate modulation in the $\alpha\beta\gamma$ frame as an alternative to the reported strategies, i.e. FS-MPC, PWM, SVM in *abc* coordinates. To the best of the author's knowledge, this is the first work where a complete SVM algorithm in $\alpha\beta\gamma$ is formally presented, analysed and experimentally validated for a four-leg NPC converter. Moreover, in this paper balancing of the capacitor voltages and selective harmonic elimination (e.g. even har-monic elimination), for a 4-leg NPC converter, is presented, fully discussed and experimentally validated.

The rest of this paper is organised as follows: In Section II the proposed modulation algorithm is discussed. In Section III a brief discussion of the control system required in the exper-imental work is presented. In Section IV experimental results are discussed and fully analysed. In Section V the conclusions and an appraisal of the proposed method are presented. Finally in the Appendices the look-up tables required in the proposed modulation algorithm are given.

II. THREE DIMENSIONAL SPACE VECTOR MODULATION FOR A FOUR-LEG NPC INVERTER

A. Four-Wire NPC Converters

In Fig. 1 the topology of a four-leg NPC converter is shown. Due to the extra leg, the four-leg NPC has several advantages in comparison to the three-leg four-wire NPC, such as: a) full dc-link utilisation, b) lower ripple in the dc-link capacitors, c) lower current through the neutral point allowing smaller dc-link capacitors and d) more levels in the output voltage with less harmonic distortion and a consequent reduction in output filter size.

The system of Fig.1 is composed of dc-link capacitors C_1 and C_2 and the switches per phase are S_{1x}, S_{2x} and $\bar{S}_{1x}$, $\bar{S}_{2x}$, where $x \in \{a, b, c, f\}$ and represents each leg of the inverter. Switches $\bar{S}_{1x}$, $\bar{S}_{2x}$ represent the complement of the switches S_{1x}, S_{2x} respectively. Each leg of the converter has three possible states $(S_{1x}, S_{2x}) \in \{(1, 1), (0, 1), (0, 0)\}$, therefore the four-leg NPC has $3^4 = 81$ switching states.

The current through the neutral-point (NP) is calculated using (1). In the rest of this paper the poles a, b and c of each leg are referred as phases, while pole f is referred as the neutral.

$$i_o = \sum_{x=a,b,c,f} \bar{S}_{1x} S_{2x} i_x \qquad (1)$$

B. Definition of the Three-Dimensional Space Vector

In order to implement SVM, a space vector transformation must be first defined and applied to the converter output voltages. For a four-leg NPC converter, a transformation to the $\alpha\beta\gamma$ coordinate system is applied to each of the 81 possible switching combinations.

$$[T]_{abc-\alpha\beta\gamma} = \frac{2}{3} \begin{bmatrix} 1 & -1/2 & -1/2 \\ 0 & \sqrt{3}/2 & -\sqrt{3}/2 \\ 1/2 & 1/2 & 1/2 \end{bmatrix} \qquad (2)$$

$$\vec{V}_{i\{\alpha,\beta,\gamma\}} = [T]_{abc-\alpha\beta\gamma} \vec{V}_{i\{abc_f\}} \qquad (3)$$

$$\vec{V}^*_{\alpha,\beta,\gamma} = [T]_{abc-\alpha\beta\gamma} \vec{V}^*_{abc_f} \qquad (4)$$

Equations (2) and (3) are solved to implement the abc_f to $\alpha\beta\gamma$ transformation, where the vector $\vec{V}_{i\{abc_f\}} = [V_{i_{af}}, V_{i_{bf}}, V_{i_{cf}}]$ of (3) represents the phase-to-neutral voltages for the ith switching combination. Note that each component of the vector $\vec{V}_{i\{abc_f\}}$ has five possible states in per-unit, i.e. $\{-2,-1,0,1,2\}$.

The 81 different switching combinations generate 65 differ-ent vectors in the $\alpha\beta\gamma$ space ($\vec{V}_{i\{\alpha,\beta,\gamma\}}$). These vectors are classified as follows: 14 redundant vectors, 50 non-redundant vectors and 1 zero vector with triple redundancy. The re-dundant vectors are those formed by two different switching combinations, but have the same representation in the $\alpha\beta\gamma$ space. For each pair of redundant vectors, the current i_o (see Fig. 1) has the same magnitude but opposite direction, this allows the voltage balance on the dc-link capacitors to

be controlled. Table A.1 in Appendix A, summarizes this information for each vector. Redundant vectors are represented as V_{xn} or V_{xp}, for $x \in [1, 14]$, where the sub-index n or p distinguishes the relative polarity of the current i_o. In addition the magnitude of each vector is presented in Table A.1 to emphasise that ten different amplitudes are present. Hence the normal classification of short, medium and long vectors, typically used for the three-leg NPC converter, is no longer applicable.

In order to synthesise a reference vector in the $\alpha\beta\gamma$ co-ordinate system with the minimum number of commutations, the nearest four vectors to the reference vector have to be identified. These four vectors form a tetrahedron, which is the smallest region that can contain the reference vector. The 65 different vectors of Table A.1, generate 192 different tetrahedrons in the $\alpha\beta\gamma$ space, which together make up the entire modulation region for the four-leg NPC as shown in Fig. 2.

In order to generate an algorithm for computing the SVM without a large number of tables, it is useful to classify each tetrahedron based on the number of non-redundant vectors they possess. In addition this classification gives a better under-standing of how the $\alpha\beta\gamma$ space is arranged for control over i_o and therefore over the dc-link capacitor voltage balance.

The tetrahedron classification is presented in Table I, where each sub-index represents the number of non-redundant vec-tors present in the tetrahedron. For instance, from Table I,
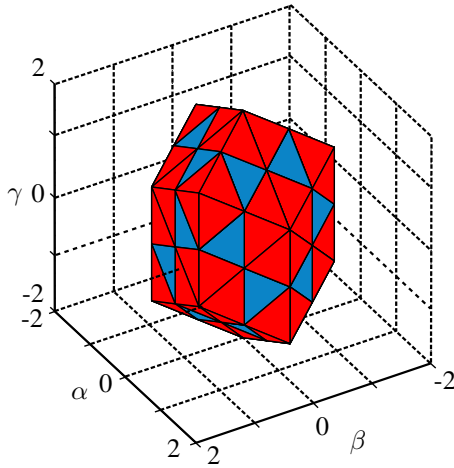

Fig. 2. Modulation region in the $\alpha\beta\gamma$ space for a four-leg NPC converter.

Tetrahedrons of type 2 (TT_2) are composed of 2 redundant vectors, 2 non-redundant vectors and there are 48 of them in the entire modulation region.

TABLE I
TETRAHEDRONS CLASSIFICATION

Tetrahedron Type (TT)	Redundant Vectors.	Non-Redundant Vectors	Zero Vectors	Total of Tetrahedrons
TT_0	3	0	1	24
TT_1	3	1	0	24
TT_2	2	2	0	48
TT_3	1	3	0	96

Figs. 3a to 3d show the internal regions of the modulation

space presented in Fig. 2. The complete region can be un-derstood as being built up from different regions, each one forming a surface and enclosing the volume of the previous one.

The first region is formed from the 24 TT_0 (and has the zero vector as its center). Fig. 3a shows this first region, composed of all the redundant vectors (i.e $\vec{V}_0$–$\vec{V}_{14}$ from Table A.1). In addition, over the surface of the region generated by the TT_0, two TT_1 are depicted to highlight how the next region is formed. Therefore a TT_1 is formed by three redundant vectors (provided by the surface of the region in Fig 3a) and another fourth vector (which must be non-redundant because all the fifteen redundant vectors form the first region). All the 24 TT_1 form the second region, which is shown in Fig. 3b. Thereupon the TT_2 are formed based on the surface of the last region. Fig. 3c shows how this is accomplished for two TT_2. Thus one TT_2 contains 2 redundant vectors and one non-redundant vector (provided by the surface generated by TT_1) and a fourth vector which must be non-redundant. The region formed by all the 48 TT_2 is depicted in Fig. 3d. Finally, and based on the same methodology, the 96 TT_3 are formed, which are shown in Fig. 2. However this region can be sub-divided into two regions, namely $TT_{3.1}$ and $TT_{3.2}$, distinguished with different colours in Fig. 2. The sub-classification of TT_3 is based on some non-redundant vectors, whose switching combinations generate zero current i_o ($\vec{V}_{30} - \vec{V}_{35}$ and $\vec{V}_{57} - \vec{V}_{64}$), this leads to two slightly different TT_3. Both of them, $TT_{3.1}$ and $TT_{3.2}$, are composed of one redundant vector and 3 non-redundant vectors, however in $TT_{3.1}$ the three non-redundant vectors generate a non-zero current i_o, while in $TT_{3.2}$ only two non-redundant vectors generate a non-zero current i_o.

C. The Reference Vector in the $\alpha\beta\gamma$ Space

The reference vector in the $\alpha\beta\gamma$ coordinate system is given by (4), where $\vec{V}^*_{abc_f} = [V^*_{af}, V^*_{bf}, V^*_{cf}]^T$ is the reference voltage vector. In the general case, the components of $\vec{V}^*_{abc_f}$ can be balanced/unbalanced and/or sinusoidal/non-sinusoidal, that can cause the reference vector $\vec{V}^*_{\alpha,\beta,\gamma}$ to describe any possible trajectory within the $\alpha\beta\gamma$ space. Assuming sinusoidal references, the voltages $\vec{V}^*_{abc_f}$ can be written as:

$$V^*_{af}(t) = m_a \frac{\sqrt{3} \cdot 2V_{dc}}{3} sin(\omega t) \tag{5}$$

$$V^*_{bf}(t) = m_b \frac{\sqrt{3} \cdot 2V_{dc}}{3} sin(\omega t - \frac{2\pi}{3}) \tag{6}$$

$$V^*_{cf}(t) = m_c \frac{\sqrt{3} \cdot 2V_{dc}}{3} sin(\omega t + \frac{2\pi}{3}) \tag{7}$$

When (5)-(7) are used to generate the voltage references, the path described by the reference vector $\vec{V}^*_{\alpha,\beta,\gamma}$ depends on the modulation index of each phase, i.e. $m_{a,b,c}$. When $m_a = m_b = m_c = m$ the trajectory of the reference vector $\vec{V}^*_{\alpha,\beta,\gamma}$ is the well known circle in the α-β plane ($\gamma = 0$). When unequal modulation indices are used, an unbalanced system is generated and the trajectory of the reference vector is an ellipse inclined in the γ axis. Fig. 4a illustrates the path, in the $\alpha\beta$ plane, described by a reference with modulation indices of $m_a = 0.95$, $m_b = 0.47$ and $m_c = 0.85$. From
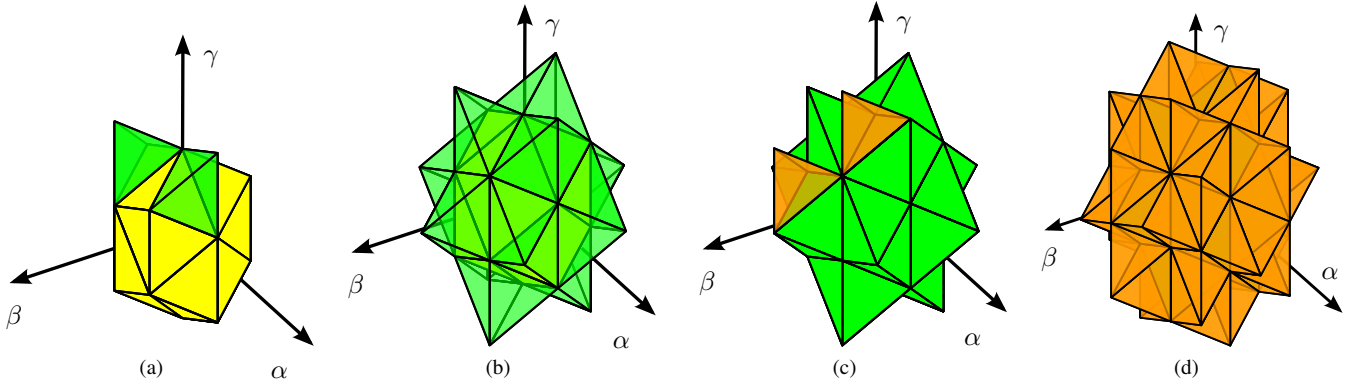
Fig. 3. Tetrahedrons definitions in the $\alpha\beta\gamma$ space for a four-leg NPC converter. In (a) the region formed by all the TT_0 and two TT_1, (b) region formed by all TT_1, (c) region formed by all the TT_1 and two TT_2, (d) region formed by all TT_2.
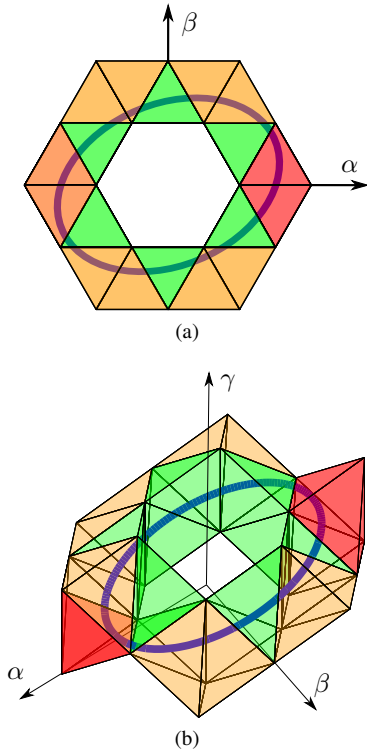

Fig. 4. Voltage reference vector path for modulation indices $m_a = 0.95, m_b = 0.47, m_c = 0.85$ in (a) the $\alpha\beta$ space and (b) the $\alpha\beta\gamma$ space.

Fig. 4a, the elliptical path, in the $\alpha\beta$ frame, and the triangles that enclose the reference vector can be clearly distinguished. Likewise Fig. 4b shows the elliptical path in the $\alpha\beta\gamma$ frame and the tetrahedrons that enclose the reference path at each sample time.

D. Synthesis of the Reference Vector

According to the trajectory followed by the reference vector $\vec{V}^*_{\alpha,\beta,\gamma}$ in the $\alpha\beta\gamma$ space, the tetrahedrons that enclose it at each sample time must be identified. Fig 5a shows the projection of Fig. 2 in the $\alpha\beta$ plane. This figure is identical to that used for the three-leg NPC modulation region, composed of 24 adjacent triangles. However for a four-leg NPC, each triangle is extended in the γ direction forming a pentahedron in the $\alpha\beta\gamma$ space. In total there are 24 pentahedrons each of them

formed by a specific number of tetrahedrons. As an example, Fig. 5b shows the pentahedron P_{m_1}, which comprises 8 different tetrahedrons.

In Fig. 5a, three types of triangles and associated pentrahedrons can be recognized. Firstly the internal-triangles, whose three dimensional projections are the pentahedrons P_{i_1}-P_{i_6}. Secondly the medium triangles that share 2 points with the internal triangles and are associated with the pentahedrons P_{m_1}-P_{m_6}. Finally the external triangles which are associated with the pentahedrons P_{e_1}-P_{e_6}. Within a particular class, i.e. P_i, P_m or P_e, all pentahedrons have the same type and number of vectors and consequently they posses the same type and number of tetrahedrons. The composition of each pentahedron is given in Table A.2. As an example, Fig. 5b shows the pentahedron P_{m_1} which comprises 11 vectors and 8 tetrahedrons. The same structure, i.e. 11 vectors and 8 tetrahedrons, is found in all the medium pentahedrons, i.e. P_{m_1}-P_{m_6} (see Table A.2).

The selection of the tetrahedron that contains the reference vector at each sample period consists of two simple steps:

a) Similarly to the traditional three-leg NPC converter, the triangle in the $\alpha\beta$ plane that encloses the $\alpha\beta$ projection of $\vec{V}^*_{\alpha,\beta,\gamma}$ is identified initially (Fig. 5a) [25]. Thus, the corresponding pentahedron of Table A.2 is selected.

b) Once the pentahedron is selected, the tetrahedron that contains $\vec{V}^*_{\alpha,\beta,\gamma}$ has to be identified. Although it could be calculated through the γ-component of the reference vector, using the voltages $\vec{V}^*_{abc_f}$ a more straightforward algorithm can be implemented. As mentioned before, each component of the vector $\vec{V}_{i\{abc_f\}}$ has five possible states in per-unit, i.e. {-2,-1,0,1,2}. Redrawing Fig. 5b, with the per-unit values marked, in Fig. 6a, it can be seen that each tetrahedron encompasses a unique range for the voltages V_{af}, V_{bf} and V_{cf}.

In the example given in Fig. 6, at a particular time t_n, the reference vector is $\vec{V}^*_{abc_f}(t_n) = [0.5, -0.3, -0.5]$. From Fig. 6a it is clear that the only tetrahedron which can contain the reference voltage is TT_1 composed of the vectors: $V_1 = [1, 0, 0]$, $V_{15} = [1, 0, -1]$, $V_4 = [0, 0, -1]$, $V_{10} = [0, -1, -1]$. Fig. 6b shows a zoom of the selected tetrahedron containing the reference vector.
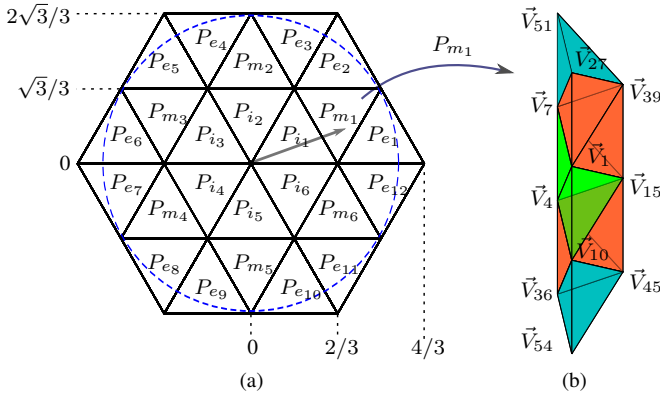
Fig. 5. Projection of the full modulation region in the α-β plane (a) and pentahedron P_{m_1} is the projection in the α-β-γ space of the triangle in the α-β plane (b).
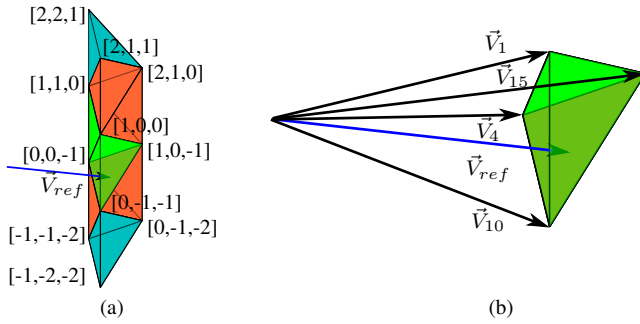

Fig. 6. In (a) the pentahedron P_{m1} with a reference vector is shown, the voltages $\vec{V}_{i\{abc_f\}}$ replace the vector $\vec{V}^*_{\alpha,\beta,\gamma}$ to allow tetrahedron identification. In (b) a close view of the selected tetrahedron is depicted.

E. Duty Cycle Calculation

Once the 4 vectors that define the selected tetrahedron have been identified, the duty cycle for each vector must be calculated. Mathematically this can be written as:

$$
\begin{bmatrix} d_1 \\ d_2 \\ d_3 \end{bmatrix} = \begin{bmatrix} V_{a-d_\alpha} & V_{b-d_\alpha} & V_{c-d_\alpha} \\ V_{a-d_\beta} & V_{b-d_\beta} & V_{c-d_\beta} \\ V_{a-d_\gamma} & V_{b-d_\gamma} & V_{c-d_\gamma} \end{bmatrix}^{-1} \begin{bmatrix} V^*_{\alpha-d} \\ V^*_{\beta-d} \\ V^*_{\gamma-d} \end{bmatrix} \tag{8}
$$

$$
d_4 = 1 - d_1 - d_2 - d_3 \tag{9}
$$

Adopting $\{\vec{V}_a, \vec{V}_b, \vec{V}_c, \vec{V}_d\}$ as the vectors that enclose the reference $\vec{V}^*_{\alpha\beta\gamma}$, (8) - (9) show the duty cycle calculation (based on the sample period T_s) for each vector. To simplify the calculation, all vectors are expressed with respect to a displaced origin located at the end of the fourth vector $\vec{V}_d$, where $\vec{V}_{i-d} = \vec{V}_i - \vec{V}_d$; $i = \{a, b, c, ref\}$. For the experimental implementation of (8), the inverse of the matrix has been calculated using the cofactor method. The equations for the cofactors and the determinant of the matrix shown in (8) are derived off-line and then programmed in the experimental system used in this work (see section IV). Therefore the terms, numerator and denominator, required for the calculation of each duty cycle d_i are calculated on-line and then divided. Calculation of the entire modulation algorithm and the associate control system occupies only 30μs of processing time in the control platform presented in Section IV.

F. Switching Sequence Definition

The selection of the switching sequence in an SVM algorithm is always a trade-off between the number of commutations, i.e. power losses, and the total harmonic distortion of the modulated waveform. In a typical two level inverter, either three or four leg, zero vectors are always used in each sample period along with the active vectors to create the reference vector. Hence, two important categories of modulation sequences can be differentiated, which mainly differ in the number of zero-vector redundancies used in the modulation [26], [27]. However in an NPC converter, either three or four leg, zero-vectors are not always present in each sample period. Hence the normal classification is no longer valid. In this paper two patterns are defined for the NPC SVM. The first one employs all possible redundancies, while the second pattern uses only one redundant vector in each sample period. In addition, only one switching state change is allowed during the transition from one vector to another. A symmetric PWM pattern is used in this work.

1) Full-Redundancy Utilisation: Four types of tetrahedrons have been defined, namely TT_0, TT_1, TT_2 and TT_3, each of which possess a different number of redundant vectors. Therefore the use of all redundancies entails a different number of commutations in each type of tetrahedron. Fig. 7a shows the switching commutation sequence for each leg of the converter and the phase-to-neutral voltages using all the possible redundancies of the TT_1 shown in Fig. 6b. Likewise Fig. 7b shows the switching commutation sequence for the TT_2 formed by $\{\vec{V}_{15}, \vec{V}_4, \vec{V}_{10}, \vec{V}_{45}\}$. As this tetrahedron possesses two redundant vectors instead of the three present in the previous example, an extra switching commutation in leg f is evident, which implies a different switching frequency in each leg of the converter.

In order to determine a suitable switching sequence using only the first column of Table A.1 and Table A.2, a simple algorithm is implemented. Table II shows the selected vectors for each of the above mentioned tetrahedrons. The vectors are arranged in decreasing amplitude with respect to the γ-component as defined in Table A.1 and are separated according to negative and positive redundancy (as non-redundant vectors possess only one switching combination, they use the entire row). The pivot vector of the sequence must be the vector that possesses the largest number of Positive(P)/Negative(N) states (marked as ●). Then starting from this point a descending/ascending direction must be followed until each vector has been transitioned once. The arrows of Table II show the sequence for each tetrahedron. This sequence is then mirrored as depicted in Fig. 7.

2) Single-Redundancy Utilisation: Although the previous switching sequence generates low THD and gives good controllability for balancing of the dc-link capacitor voltage, it employs a high switching frequency and a different switching frequency for each leg of the converter, which in some cases may be unacceptable. In order to reduce the switching frequency, a method employing single redundancy has been developed. At least one redundancy must be used, because it allows control over the dc-link voltage balance, and the
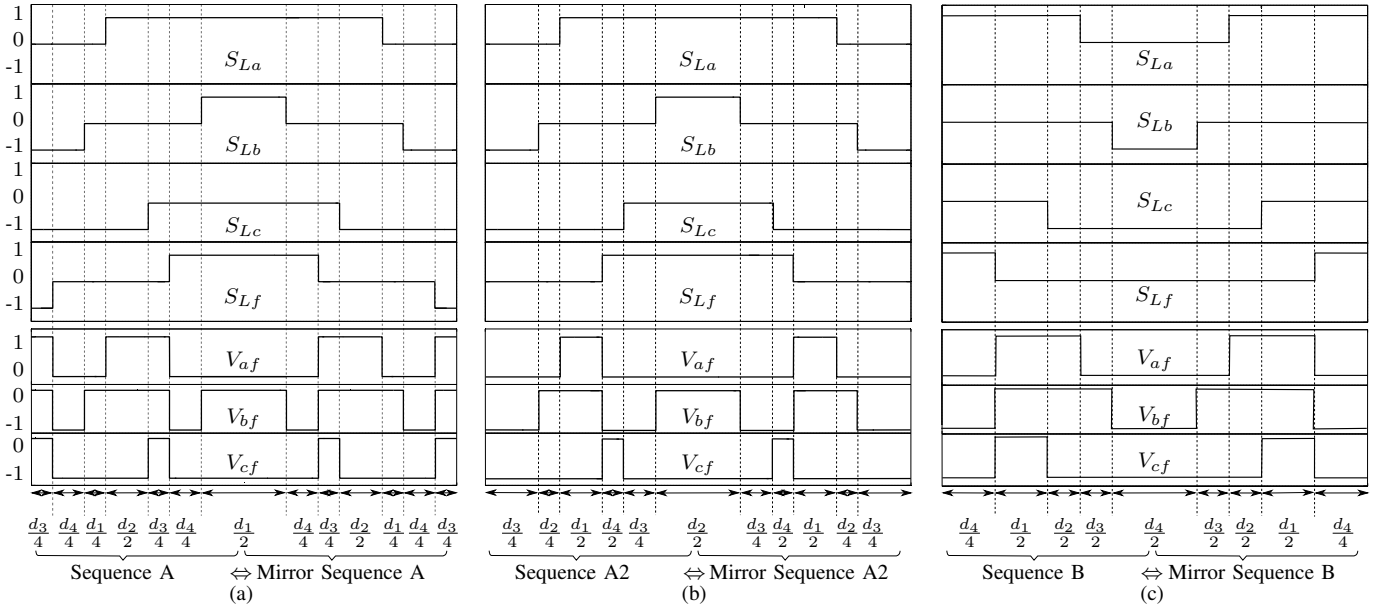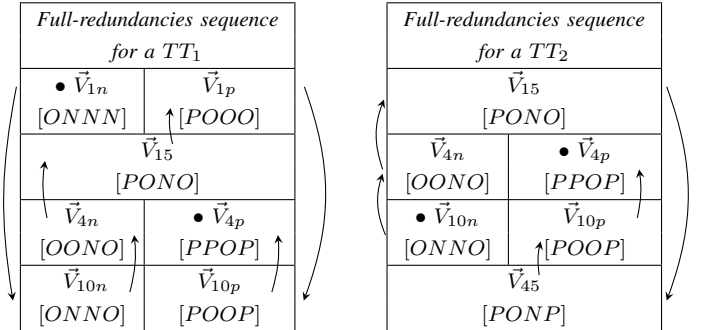
Fig. 7. Switching commutation for each leg of the four-leg NP converter and the phase-to-neutral output voltages for: (a) full-redundancies sequence for a TT_1 formed by $\{\vec{V}_1, \vec{V}_{15}, \vec{V}_4, \vec{V}_{10}\}$, which sequence is: $\{\vec{V}_{1n} - \vec{V}_{10n} - \vec{V}_{4n} - \vec{V}_{15} - \vec{V}_{1p} - \vec{V}_{10p} - \vec{V}_{4p}\} \Leftrightarrow Mirror$, (b) full-redundancies sequence for a TT_2 formed by $\{\vec{V}_{15}, \vec{V}_4, \vec{V}_{10}, \vec{V}_{45}\}$, which sequence is: $\{\vec{V}_{10n} - \vec{V}_{4n} - \vec{V}_{15} - \vec{V}_{45} - \vec{V}_{10p} - \vec{V}_{4p}\} \Leftrightarrow Mirror$ and (c) one-redundancy sequence for the same TT_1 of (a), using $\vec{V}_{10p}$ as pivot, where the sequence is: $\{\vec{V}_{10p} - \vec{V}_{1p} - \vec{V}_{15} - \vec{V}_{4n} - \vec{V}_{10n}\} \Leftrightarrow Mirror$.

redundancy with the largest duty cycle is selected at each sample time. The sequence pattern is based on the same algorithm as explained above. However the algorithm stops once it reaches the pivot vector redundancy. Thus for example in the TT_1 and using $\vec{V}_{4n}$ as the pivot, the correct sequence is: "$\vec{V}_{4n} - \vec{V}_{15} - \vec{V}_{1p} - \vec{V}_{10p} - \vec{V}_{4p} \Leftrightarrow Mirror$". Using $\vec{V}_{10p}$ as the pivot, then the sequence is: "$\vec{V}_{10p} - \vec{V}_{1p} - \vec{V}_{15} - \vec{V}_{4n} - \vec{V}_{10n} \Leftrightarrow Mirror$". This last sequence is shown in Fig. 7c, where only one switching commutation per sample time in each leg is ensured. Furthermore, by always using the same type of redundancy (positive or negative) as the pivot, an extra switching commutation when moving from one tetrahedron to another is avoided. This sequence pattern yields a switching frequency equal to half the sampling frequency for each switch of the converter. This is true also for the fourth leg which has to modulate a signal with a frequency of three times the fundamental frequency to achieve sinusoidal voltages at the converter output. In some applications, it is desirable to alternate the type of redundancy every 60 degrees, this eliminates even harmonics which are very undesirable in grid connected applications. This is achieved with a negligible increment of the switching frequency.

G. Capacitor Voltage Balance

Different techniques to balance the voltages on the dc-link capacitors have been reported in the literature for the conventional three-level, three-leg NPC converter. These are usually categorised as active control, passive control and hysteresis control. [28], [29], [30]. In this work an active control methodology, embedded into the utilisation and selection of the SVM redundant vectors, is proposed to balance the capacitor voltages. According to this, a Pulse Width Modulation technique is applied, at each sample time, to the redundant

TABLE II
SWITCHING SEQUENCE PATTERN.

Full-redundancies sequence for a TT_1	
• $\vec{V}_{1n}$ [ONNN]	$\vec{V}_{1p}$ ↑[POOO]
$\vec{V}_{15}$ [PONO]	
$\vec{V}_{4n}$ [OONO] ↑	• $\vec{V}_{4p}$ [PPOP] ↑
$\vec{V}_{10n}$ [ONNO]	$\vec{V}_{10p}$ [POOP]

Full-redundancies sequence for a TT_2	
$\vec{V}_{15}$ [PONO]	
$\vec{V}_{4n}$ [OONO]	• $\vec{V}_{4p}$ [PPOP] ↑
• $\vec{V}_{10n}$ [ONNO]	$\vec{V}_{10p}$ ↑[POOP]
$\vec{V}_{45}$ [PONP]	

vectors in order to modulate the neutral point current i_o to track a reference current (i_o^*) and balance the voltages on the dc-link capacitors V_{C_1} and V_{C_2}. The reference current i_o^* is provided by an external controller, which is presented in the next section. Adopting $\{\vec{V}_a, \vec{V}_b, \vec{V}_c, \vec{V}_d\}$ as the four vectors that form a specific tetrahedron, the averaged NP current in one sample period can be mathematically expressed as:

$$i_o^* = \lambda_a \cdot d_1 \cdot i_{o_a}(\vec{V}_a) + \lambda_b \cdot d_2 \cdot i_{o_b}(\vec{V}_b) + \quad (10)$$
$$\lambda_c \cdot d_3 \cdot i_{o_c}(\vec{V}_c) + \lambda_d \cdot d_4 \cdot i_{o_d}(\vec{V}_d)$$

$$\left.\begin{array}{rl} d_{k_p} = & (1 + \lambda_i) \cdot \frac{d_k}{2} \\[2mm] d_{k_n} = & (1 - \lambda_i) \cdot \frac{d_k}{2} \\[2mm] |\lambda_i| \leq & 1 \end{array}\right\} \quad \begin{array}{l} i \in \{a, b, c, d\} \\ k \in \{1, 2, 3, 4\} \end{array} \quad (11)$$

where $i_{o_i}(\vec{V}_i)$ represent the currents through the NP generated for each vector and are determined using (1), d_i are the
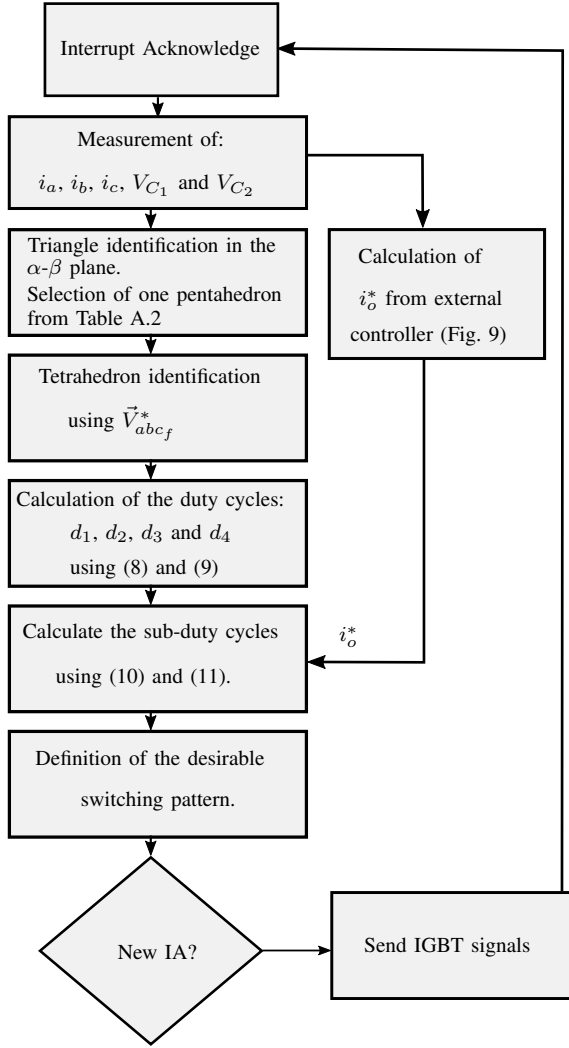
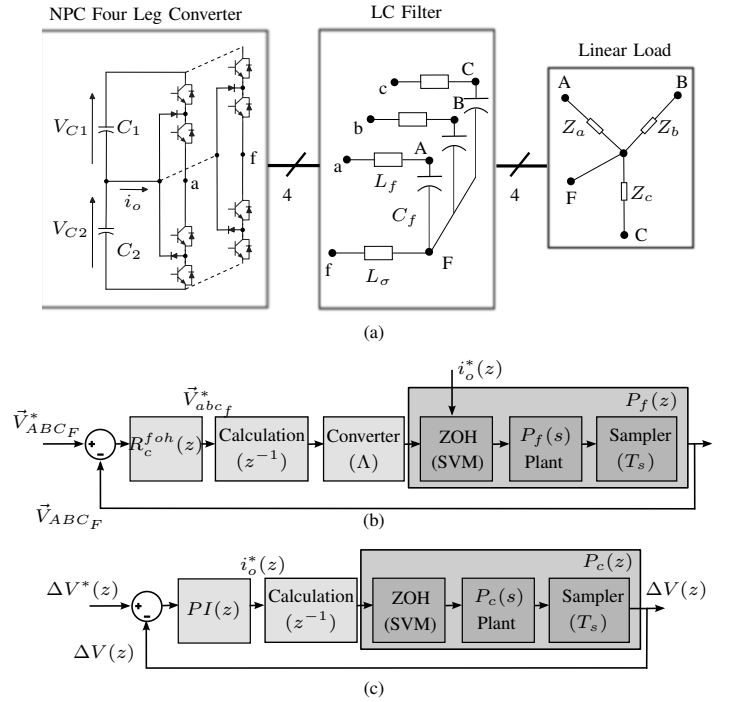Fig. 8. Flowchart of 3D-SVM for a four-leg NPC converter.

Fig. 9. Control scheme for the regulation of the output voltage and balance on the dc-link capacitor for a four-leg NPC converter.

III. PROPOSED RESONANT VOLTAGE CONTROLLER

To experimentally validate the proposed modulation scheme, a prototype converter was constructed and used to feed an unbalanced three-phase load connected through an *LC* filter as shown in Fig. 9a. An additional optional inductance L_σ is considered in the fourth leg. The linear unbalanced load is composed of impedances Z_a, Z_b and Z_c. .

It is well-known that conventional PI controllers are not particularly suited to regulate sinusoidal signals [10] [31] [32]. On the other hand, and according to the internal model principle [10], resonant controllers can regulate, with zero steady state error, sinusoidal voltages and currents [32]. Therefore, to control the output voltages of the 4-leg NPC converter, the utilisation of resonant controllers is proposed in this work.

Fig. 9b presents the proposed control systems for regulation of the converter output voltage. In this diagram the converter is represented as a constant gain Λ, the modulation algorithm and the computational delay are represented by a unit delay (z^{-1}) cascaded with a Zero Order Hold (ZOH). The worst case situation (from the control design viewpoint) is when the converter output is unloaded and the plant $P_f(s)$ is solely represented by the lightly-damped *LC* output power filter. To simplify the analysis in the frequency domain, the control system is designed in the s-domain considering the transfer function of a resonant controller with delay compensation (see [33],[31]).

$$R^c(s) = \sum_{n=1}^{k} R_n^c(s) = \sum_{n=1}^{k} K_n \frac{s \cos\vartheta_n - \omega_n \sin\vartheta_n}{s^2 + \omega_n^2} \quad (12)$$

where ω_n represents the nth controlled frequency. The angle ϑ_n represents the phase shift between the voltage modulated

duty cycles calculated in (8)-(9) and λ_i represents the sub-modulation indices, which are calculated in order to obtain an average current equal to i_o^*. Each redundant vector allows modulation of the current generated through the NP by adjusting the duty cycles of each redundancy (positive and negative), this allows the sub-modulation index $\lambda_i \in [-1, 1]$. As (10) is a general representation, the sub-modulation index λ_i must be set to 1 for non-redundant vectors. Additionally, each current $i_{o_i}(\vec{V}_i)$ must be calculated from (1) or obtained from a Look-Up Table (LUT) stored in the third column of Table A.1. Equation (11) shows the calculation of the sub-duty cycles for the redundant vectors, where d_{k_p} and d_{k_n} represent the sub-duty cycle for the positive and negative redundancy of the redundant vector. The number of indices λ_i and sub-duty cycle calculations is equal to the number of redundant vectors present in the selected tetrahedron. When the switching sequence: *Single-Redundancy Utilisation* of section II is used, only one sub-duty cycle needs to be calculated at each sample time. Finally, the diagram of Fig. 8 shows the required steps to implement the proposed SVM algorithm for a four-leg NPC converter with capacitor voltage balancing.

by the converter and the voltage regulated at the output. Notice that ϑ_n is a function of the frequency ω_n and considers the phase shifts introduced by the proposed SVM (one sample period delay), the phase shift introduced by the plant $P_f(s)$ transfer function, etc.

Notice that compensation of the system phase shift angle ϑ_n, in (12) is one of the methods used to compensate the phase margin of the open loop transfer function $G(s) = R^c(s)P_f(s)$ without using additional lead-lag networks (see [33],[31]).

The plant transfer function $P_f(s)$, considering only the second order LC output power filter, is obtained as:

$$P_f(s) = \frac{V_{abc_f}(s)}{V_{ABC_F}(s)} = \frac{1}{L_f C_f s^2 + R_f C_f s + 1} \quad (13)$$

where L_f and R_f represent the inductance with its intrinsic resistance and C_f is the filter capacitance. Using Fig. 9b, and the plant of (13), the controller gain (K_n in (12)) can be designed. To discretise the s-plane controller of (12), maintaining most of its original performance, the First Order Hold (FOH) discretisation method is used (see [31]).

Using the Nyquist plot, the discrete time performance of the resonant controller can be analysed using the diagram depicted in Fig. 10. From this figure, it is observed that the plot does not encircle the point $(-1, 0j)$ ensuring a stable operation. Its stability margin is usually defined by the minimum distance from the plot of $G(s)$ to the point $(-1, 0j)$ [32] (see η in Fig. 10), which in this design is set to 0.51 (see [32]). Besides analysing the stability and dynamic performance of the proposed control system, the Nyquist plot of Fig. 10 could also be used for fine adjustment of the controller parameters (see (12)), for instance the gain K_n.
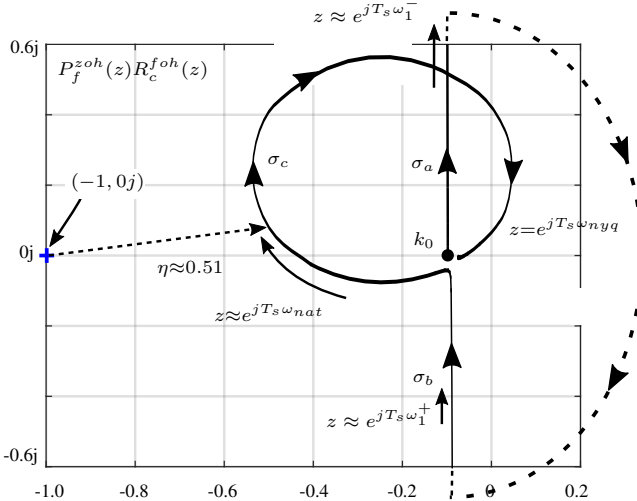
Fig. 10. Nyquist diagram for design of the resonant controller $R_c^{foh}(z)$. For $R_c^{foh}(z)$: $\omega_1 = 100\pi\,\mathrm{rad\,s^{-1}}$, $K_1 = 70$, $D_1 = 1.54$. For $P_f^{zoh}(z)$: $L_f = 1\,\mathrm{mH}$, $C_f = 67\,\mathrm{\mu F}$, $R_f = 0.1\,\Omega$. $T_s = 1/6000\,\mathrm{s}$, $\omega_{nyq} = 6000\pi\,\mathrm{rad\,s^{-1}}$, $\omega_{nat} = 3863\,\mathrm{rad\,s^{-1}}$.

In order to balance the dc-link capacitor voltages, the reference current $i_o^*(z)$ is obtained at the output of a PI controller and used to calculate the sub-duty cycles of (11). Accordingly, Fig. 9c shows the proposed control scheme to regulate the dc-link capacitor voltages. Considering $C_1 \approx C_2$, the discrete

form of the plant $P_c(s)$, which relates the difference of the voltages V_{C_1} and V_{C_2} to the current i_o, is given by:

$$P_c(z) = \frac{V_{C_1}(z) - V_{C_2}(z)}{i_o(z)} = \frac{\Delta V(z)}{i_o(z)} = \frac{T_s}{C(z-1)} \quad (14)$$

using (14) the design of the *PI* controller utilising linear control design methods (e.g. root locus) is simple to achieve.

IV. EXPERIMENTAL VALIDATION

A. Experimental Set-up

The experimental rig used to validate the proposed 3D-SVM in a four-leg NPC is shown in Fig 11 (load is not shown).

The control platform is based on a Pentium-System board (2Gb RAM host PC with a 3.2GHz Pentium processor running the Arch-Linux operating system) and an FPGA board. This Pentium system runs the algorithm in real time using the Real Time Application Interface (RTAI) for Linux and is connected to the FPGA board using an ISA-bus. The FPGA board receives the measured states, implements over-voltage and over-current protection, implements the commutation dead time and sends the control signals to the IGBTs. The gate-signals are sent through optical fibers from the FPGA board to the 4-leg NPC.

The 4LNPC converter is based on the Microsemi IGBT-APTGL60TL120T3G, $60A$ and $1200V$. The experimental data has been acquired using a Textronix DPO 2024 Digital Phosphor Osciloscope, 200MHz, 1GS/s.
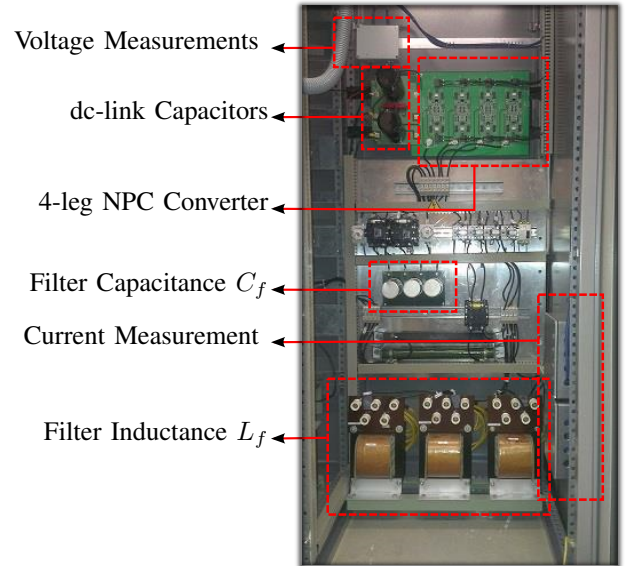
Fig. 11. Experimental rig for a four-leg NPC converter

B. Experimental Results

In order to demonstrate successful implementation of the proposed modulation scheme, three different experimental assessments are performed. First the system is operated in open loop control using a low switching frequency. The aims of these tests is to show experimental results related mainly

to the performance of the modulation algorithm with and without considering even harmonic elimination. Secondly the control scheme of Fig. 9 is implemented and experimentally tested considering the proposed SVM algorithm operating with balanced and unbalanced loads.

Table III shows the parameters used in the experimental implementation (Notice that $V_{dc} = V_{C1} + V_{C2}$). All experimental tests have been performed with the $Single - Redundancy$ pattern, discussed in section II.

TABLE III
GENERAL PARAMETERS OF THE IMPLEMENTED SYSTEMS

Parameter	Value	Parameter	Value
C_1	3300 uF	Za_1	$52\,\Omega$; $10\,mH$
C_2	3300 uF	Zb_1	$52\,\Omega$; $10\,mH$
V_{dc}	545 V	Zc_1	$52\,\Omega$; $10\,mH$
C_f	67 uF	Za_2	$75\,\Omega$; $10\,mH$
L_f	1 mH	Zb_2	$52\,\Omega$; $10\,mH$
L_σ	0.1 mH	Zc_2	$85\,\Omega$; $10\,mH$

1) Open-Loop Voltage Modulation: In order to reduce the harmonic content of the modulated waveform, quarter-wave and half-wave symmetry is required. For this purpose the reference waveform must be symmetrically sampled and the switching frequency must be a multiple of six times the fundamental frequency. Hence $f_{SVM} = 6 \cdot n \cdot 50Hz$. For this test $f_{SVM} = 1200Hz$ has been used in the algorithm and the load is disconnected. Fig. 12a and Fig12b show the phase-to-neutral output voltage of the four-leg NPC converter without and with the even harmonic elimination respectively. The differences in the symmetry can be cleared observed. In addition, Fig. 13a and Fig. 13b show the corresponding Fast-Fourier-Transform (FFT) for each waveform. Although even harmonics are eliminated, odd harmonics such as the 19th, 29th, 31st, 39th and 41th for instance are increased. Nevertheless, the algorithm with even harmonic elimination is preferable when grid connection is required [24].

2) Closed-Loop Voltage Controller: In order to implement a high performance three-phase voltage source for four-wire systems, the control diagram of Fig. 9 has been implemented. The full algorithm, including voltage balance of the dc-link capacitors and the implementation of the resonant close loop control system takes approximately $30\mu s$ to be executed. Fig. 14b and 14a shows the output voltage and currents for a balanced load impact of $3kW$. The output voltage is regulated to $220Vrms$ and the parameters of Table III have been used with the balanced load, i.e. Z_{a1}, Z_{b1} and Z_{c1}.

The voltage remains sinusoidal with well regulated amplitude before and after the load impact confirming the fast transient response of the control scheme. Finally and similar to the previous test, the output voltage is regulated to $220Vrms$ using the control diagram of Fig. 9. The parameters used for this test are shown in Table III, however the unbalanced load: Z_{a2}, Z_{b2} and Z_{c2} has been used. Figs. 15b and 15a show the output voltages and currents, generated by a load impact of $0.65kW$, $1kW$ and $0.57kW$ for each phase. Additionally the voltage on the dc-link capacitors is shown in Fig. 15c. The dc link voltage waveform changes noticeably after the load impact is applied. The increased ripple after the load impact
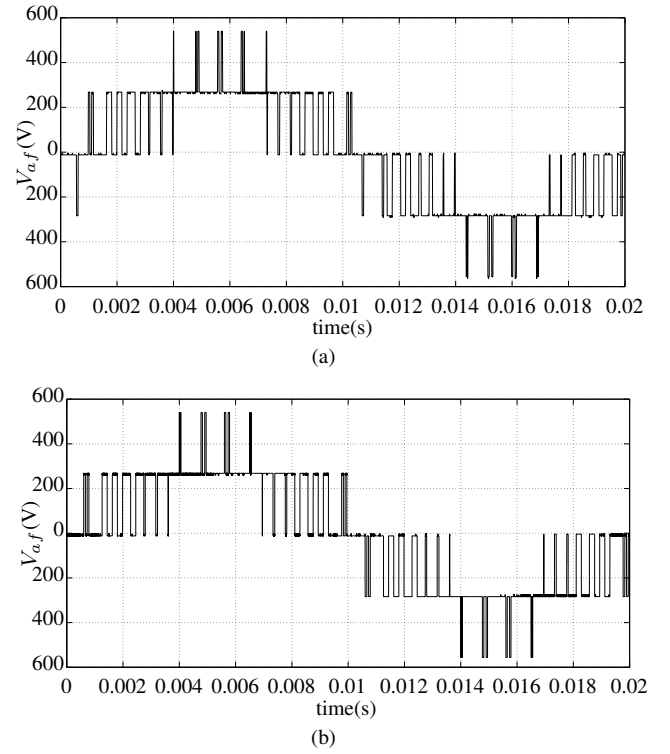
Fig. 12. Experimental assessment of 3D-SVM for a four-leg NPC (a) V_{af} without even-harmonic eliminations and (b) V_{af} with even-harmonic elimination. Measurements are with the load disconnected, $f_{SVM} = 1200Hz$, $m = 0.95$ and $V_{dc} = 545V$.
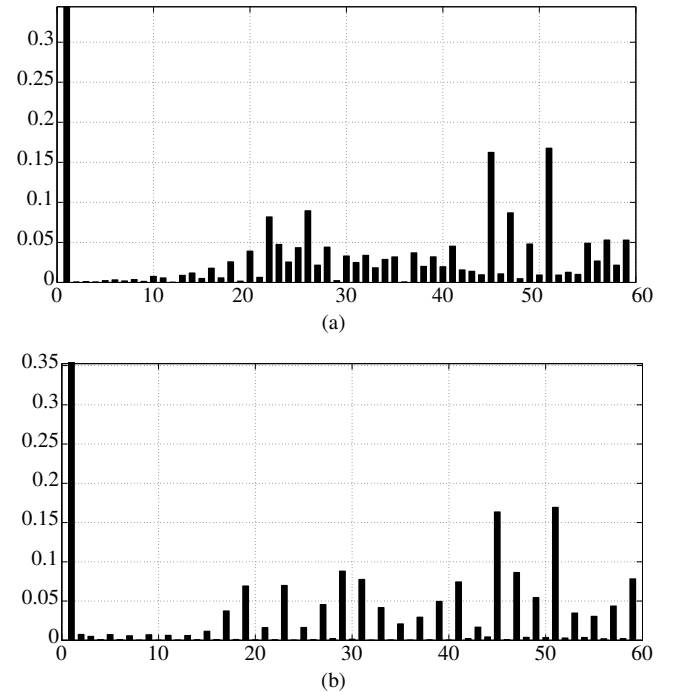
Fig. 13. Normalized amplitude of harmonic components based on 50Hz fundamental frequency. The Discrete-Fourier-Transformation (DFT) is calculated until the 60th harmonic for the waveform of (a) Fig.12a and (b) Fig. 12b.

is produced by the unbalanced currents, however active control over the voltage of the dc-link capacitors maintains the voltage difference within a tolerance smaller than $3V$.
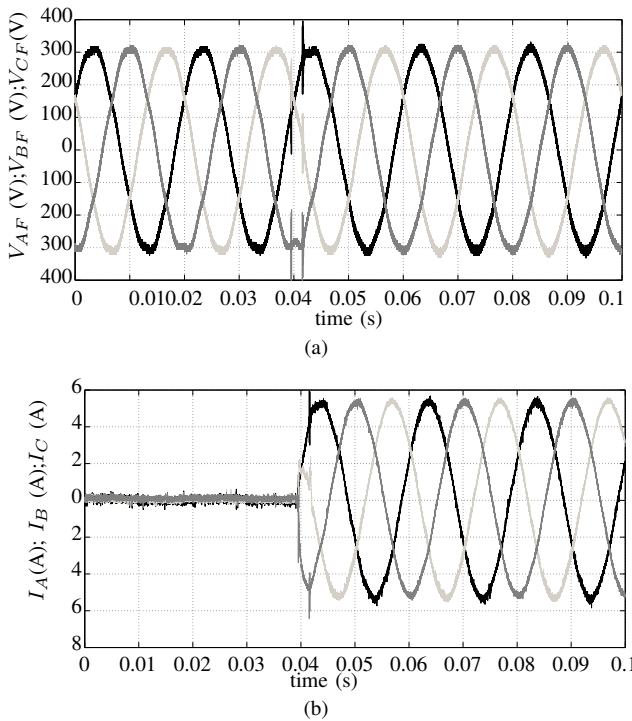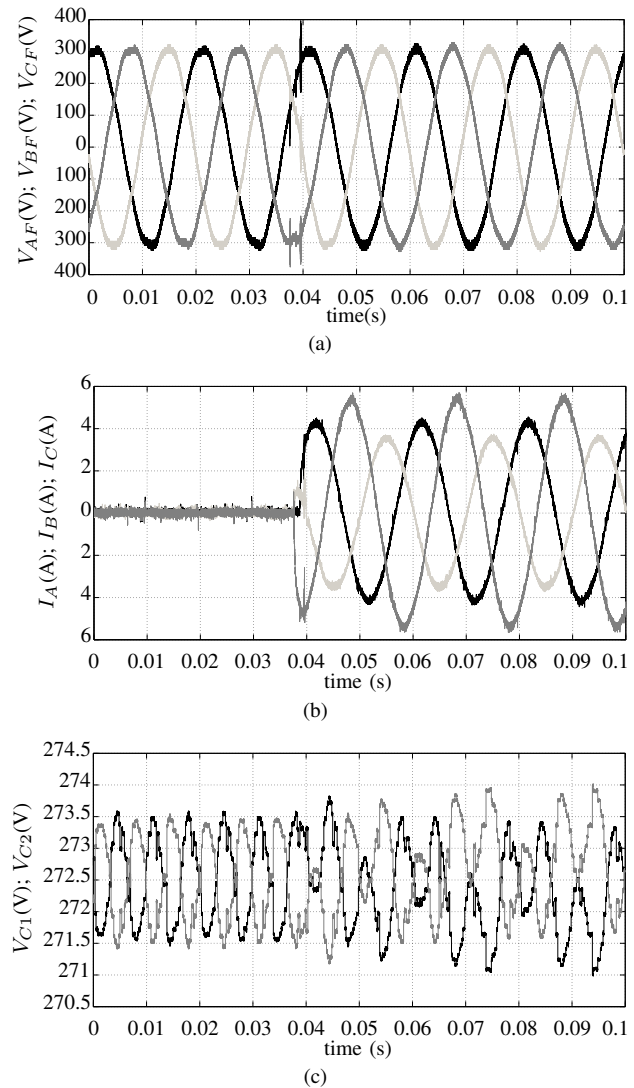
Fig. 14. Experimental assessment for a balanced load impact and voltage regulation to $220Vrms$. In (a) the output voltages are shown, (b) shows the load currents.

V. CONCLUSIONS

This paper has presented a comprehensive analysis, formulation and experimental validation of a Three-Dimensional Space Vector Modulation for a three-level, four-leg NPC Converter. A simple algorithm for implementing the proposed modulation scheme as well as achieving dc-link capacitor voltage balancing has been developed and experimentally validated. The modulation algorithm is formulated in a general form, thereby allowing different sequence patterns for the modulation and for the balance of the dc-link voltage capacitors using a various numbers of redundant vectors. Implementation of the algorithm does not require extensive use of look-up tables.

In order to meet standards for grid connected applications, even harmonic elimination is simple to achieve with the proposed SVM algorithm. This has been experimentally validated. Finally, the proposed modulation algorithm has been used in a closed-loop system based on a PR-controller, regulating the output voltage of the four-leg NPC converter. This configuration achieves both very good dynamic and steady-state performance and represents an attractive solution for a high performance power interface for four-wire applications.

APPENDIX A
3D-SVM VECTORS TABLE

REFERENCES

[1] H. R. Teymour, D. Sutanto, K. M. Muttaqi, and P. Ciufo, "Solar PV and battery storage integration using a new configuration of a three-level NPC inverter with advanced control strategy," *IEEE Transactions on Energy Conversion*, vol. 29, no. 2, pp. 354–365, 2014.

Fig. 15. Experimental assessment for a unbalanced load impact and voltage regulation to $220Vrms$. In (a) the output voltages are shown, (b) shows the load currents and (c) voltages on the dc-link capacitors.

[2] U. M. Choi, H. H. Lee, and K. B. Lee, "Simple neutral-point voltage control for three-level inverters using a discontinuous pulse width modulation," *IEEE Transactions on Energy Conversion*, vol. 28, no. 2, pp. 434–443, 2013.

[3] N.-c. I. Systems, U.-m. Choi, S. Member, J.-s. Lee, and S. Member, "New Modulation Strategy to Balance the Neutral-Point Voltage for Three-Level," *IEEE Trans. on Energy Conversion*, vol. 29, no. 1, pp. 91–100, 2014.

[4] M. Liserre, R. Cardenas, M. Molinas, and J. Rodriguez, "Overview of Multi-MW Wind Turbines and Wind Parks," *IEEE Transactions on Industrial Electronics*, vol. 58, no. 4, pp. 1081–1095, apr 2011.

[5] S.-j. Chee, H.-s. Kim, and S.-k. Sul, "Common-mode Voltage Reduction of Three Level Four Leg PWM Converter," in *IEEE Energy Conversion Congress and Exposition ECCE 2014.*, 2014, pp. 187–194.

[6] E. Bueno, S. Cobreces, F. Rodriguez, A. Hernandez, and F. Espinosa, "Design of a Back-to-Back NPC Converter Interface for Wind Turbines With Squirrel-Cage Induction Generator," *IEEE Transactions on Energy Conversion*, vol. 23, no. 3, pp. 932–945, sep 2008.

[7] C. Xia, X. Gu, T. Shi, and Y. Yan, "Neutral-point potential balancing of three-level inverters in direct-driven wind energy conversion system," *IEEE Transactions on Energy Conversion*, vol. 26, no. 1, pp. 18–29, 2011.

[8] O. Vodyakho and C. C. Mi, "Three-Level Inverter-Based Shunt Active Power Filter in Three-Phase Three-Wire and Four-Wire Systems," *Power Electronics, IEEE Transactions on*, vol. 24, no. 5, pp. 1350–1363, may 2009.

TABLE A.1
THE 81 DIFFERENT SWITCHING COMBINATIONS FOR A 4-LEG NPC
CONVERTER IN THE α-β-γ SPACE.(P=1, O=0 AND N=-1)

Space Vector $\vec{V}_{i\{\alpha\beta\gamma\}}$	Switching Combination $[S_{La}...S_{Lf}]$	Current $i_{o_i}(\vec{V}_{i\{\alpha\beta\gamma\}})$	Vector Size (p.u.) $|\vec{V}_{i\{\alpha\beta\gamma\}}|$	Vector Classification
$\vec{V}_{0z}$	[OOOO]	0		
$\vec{V}_{0p}$	[PPPP]	0	0	Zero Vec.
$\vec{V}_{0n}$	[NNNN]	0		
$\vec{V}_{1n}$	[ONNN]	ia		
$\vec{V}_{1p}$	[POOO]	-ia		
$\vec{V}_{2n}$	[NONN]	ib		
$\vec{V}_{2p}$	[OPOO]	-ib		
$\vec{V}_{3n}$	[NNON]	ic		
$\vec{V}_{3p}$	[OOPO]	-ic		
$\vec{V}_{4n}$	[OONO]	-ic	$\frac{\sqrt{5}}{3}$	
$\vec{V}_{4p}$	[PPOP]	ic		
$\vec{V}_{5n}$	[ONOO]	-ib		
$\vec{V}_{5p}$	[POPP]	ib		
$\vec{V}_{6n}$	[NOOO]	-ia		
$\vec{V}_{6p}$	[OPPP]	ia		
$\vec{V}_{7n}$	[OONN]	ia + ib		
$\vec{V}_{7p}$	[PPOO]	- ia - ib		Redundant Vec.
$\vec{V}_{8n}$	[ONON]	ia + ic		
$\vec{V}_{8p}$	[POPO]	- ia - ic		
$\vec{V}_{9n}$	[NOON]	ib + ic		
$\vec{V}_{9p}$	[OPPO]	- ib - ic		
$\vec{V}_{10n}$	[ONNO]	- ib - ic		
$\vec{V}_{10p}$	[POOP]	ib + ic	$\frac{\sqrt{2}}{3}$	
$\vec{V}_{11n}$	[NONO]	- ia - ic		
$\vec{V}_{11p}$	[OPOP]	ia + ic		
$\vec{V}_{12n}$	[NNOO]	- ia - ib		
$\vec{V}_{12p}$	[OOPP]	ia + ib		
$\vec{V}_{13n}$	[OOON]	ia + ib + ic		
$\vec{V}_{13p}$	[PPPO]	- ia - ib - ic	1	
$\vec{V}_{14n}$	[NNNO]	- ia - ib - ic		
$\vec{V}_{14p}$	[OOOP]	ia + ib + ic		

TABLE
CONTINUATION TABLE A.1

Space Vector $\vec{V}_{i\{\alpha\beta\gamma\}}$	Switching Combination $[S_{La}...S_{Lf}]$	Current $i_{o_i}(\vec{V}_{i\{\alpha\beta\gamma\}})$	Vector Size (p.u.) $|\vec{V}_{i\{\alpha\beta\gamma\}}|$	Vector Classification
$\vec{V}_{15}$	[PONO]	- ia - ic		
$\vec{V}_{16}$	[OPNO]	- ib - ic		
$\vec{V}_{17}$	[PNOO]	- ia - ib	$\frac{2\sqrt{3}}{3}$	
$\vec{V}_{18}$	[ONPO]	- ib - ic		
$\vec{V}_{19}$	[NPOO]	- ia - ib		
$\vec{V}_{20}$	[NOPO]	- ia - ic		
$\vec{V}_{21}$	[PPNO]	- ia - ib - ic		
$\vec{V}_{22}$	[PNPO]	- ia - ib - ic		
$\vec{V}_{23}$	[NPPO]	- ia - ib - ic	$2\frac{\sqrt{17}}{6}$	
$\vec{V}_{24}$	[PNNO]	- ia - ib - ic		
$\vec{V}_{25}$	[NPNO]	- ia - ib - ic		
$\vec{V}_{26}$	[NNPO]	- ia - ib - ic		
$\vec{V}_{27}$	[POON]	ib + ic		
$\vec{V}_{28}$	[OPON]	ia + ic		
$\vec{V}_{29}$	[OOPN]	ia + ib		
$\vec{V}_{30}$	[PNNN]	0		
$\vec{V}_{31}$	[NPNN]	0		
$\vec{V}_{32}$	[NNPN]	0	$\frac{2\sqrt{5}}{3}$	
$\vec{V}_{33}$	[PPNP]	0		Non-red. Vec.
$\vec{V}_{34}$	[PNPP]	0		
$\vec{V}_{35}$	[NPPP]	0		
$\vec{V}_{36}$	[OONP]	ia + ib		
$\vec{V}_{37}$	[ONOP]	ia + ic		
$\vec{V}_{38}$	[NOOP]	ib + ic		
$\vec{V}_{39}$	[PONN]	ib		
$\vec{V}_{40}$	[OPNN]	ia		
$\vec{V}_{41}$	[PNON]	ic		
$\vec{V}_{42}$	[ONPN]	ia		
$\vec{V}_{43}$	[NPON]	ic		
$\vec{V}_{44}$	[NOPN]	ib	$2\frac{\sqrt{21}}{6}$	
$\vec{V}_{45}$	[PONP]	ib		
$\vec{V}_{46}$	[OPNP]	ia		
$\vec{V}_{47}$	[PNOP]	ic		
$\vec{V}_{48}$	[ONPP]	ia		
$\vec{V}_{49}$	[NPOP]	ic		
$\vec{V}_{50}$	[NOPP]	ib		
$\vec{V}_{51}$	[PPON]	ic		
$\vec{V}_{52}$	[POPN]	ib		
$\vec{V}_{53}$	[OPPN]	ia	$2\frac{\sqrt{29}}{6}$	
$\vec{V}_{54}$	[ONNP]	ia		
$\vec{V}_{55}$	[NONP]	ib		
$\vec{V}_{56}$	[NNOP]	ic		
$\vec{V}_{57}$	[PPNN]	0		
$\vec{V}_{58}$	[PNPN]	0		
$\vec{V}_{59}$	[NPPN]	0	$\frac{4\sqrt{2}}{3}$	
$\vec{V}_{60}$	[PNNP]	0		
$\vec{V}_{61}$	[NPNP]	0		
$\vec{V}_{62}$	[NNPP]	0		
$\vec{V}_{63}$	[PPPN]	0	2	
$\vec{V}_{64}$	[NNNP]	0		

[9] R. Zhang, V. Prasad, D. Boroyevich, and F. Lee, "Three-dimensional space vector modulation for four-leg voltage-source converters," *IEEE Transactions on Power Electronics*, vol. 17, no. 3, pp. 314–326, may 2002.

[10] R. Cardenas, E. Espina, J. Clare, and P. Wheeler, "Self-tuning resonant control of a seven-leg back-to-back converter for interfacing variable-speed generators to four-wire loads," *IEEE Transactions on Industrial Electronics*, vol. 62, no. 7, pp. 4618–4629, July 2015.

[11] J.-H. Kim and S.-K. Sul, "A Carrier-Based PWM Method for Three-Phase Four-Leg Voltage Source Converters," *IEEE Transactions on Power Electronics*, vol. 19, no. 1, pp. 66–75, jan 2004.

[12] M. Perales, M. Prats, R. Portillo, J. Mora, J. Leon, and L. Franquelo, "Three-dimensional space vector modulation in abc coordinates for four-leg voltage source converters," *IEEE Power Electronics Letters*, vol. 99, no. 4, pp. 104–109, dec 2003.

[13] M. Rivera, V. Yaramasu, Llor, ., J. Rodriguez, B. Wu, and M. Fadel, "Digital Predictive Current Control of a Three-Phase Four-Leg Inverter," 2012.

[14] R. Cardenas, R. Pena, P. Wheeler, and J. Clare, "Experimental Validation of a Space-Vector-Modulation Algorithm for Four-Leg Matrix Converters," *IEEE Transactions on Industrial Electronics*, vol. 58, no. 4, pp. 1282–1293, apr 2011.

[15] P. W. Wheeler, P. Zanchetta, J. C. Clare, L. Empringham, M. Bland, and D. Katsis, "A Utility Power Supply Based on a Four-Output Leg Matrix Converter," *IEEE Transactions on Industry Applications*, vol. 44, no. 1, pp. 174–186, 2008.

[16] P. Cortes, D. O. Boillat, and J. W. Kolar, "Phase-oriented control of

a modular 3-Phase 3-level 4-leg inverter AC power source supplying floating or grounded loads," *IEEE Energy Conversion Congress and Exposition, ECCE 2013*, pp. 1357–1363, 2013.

[17] S.-j. Chee and S.-k. Sul, "Loss comparison of the 3 level topologies for

---

Roberto Cárdenas (S'95-M'97-SM'07) was born in Punta Arenas Chile. He received his B.S. degree from the University of Magallanes, Chile, in 1988 and his Msc. and Ph.D degrees from the University of Nottingham in 1992 and 1996 respectively. From 1989-1991 and 1996-2008 he was a lecturer in the University of Magallanes Chile. From 1991 to 1996 he was with the Power Electronics Machines and Control Group (PEMC group), University of Nottingham, United Kingdom. From 2009-2011 he was with the Electrical Engineering Department, University of Santiago. He is currently a professor in power electronics and drives with the Electrical Engineering Department, University of Chile, Chile. He received the Best Paper Award from the IEEE TRANSACTIONS ON INDUSTRIAL ELECTRONICS in 2005. His main interests are in control of electrical machines, variable speed drives and renewable energy systems. Professor Crdenas is a senior member of the Institute of Electrical and Electronic Engineers.

Ricardo Repenning (S'11-M'16) was born in Chile in 1988. He received the B.E. degree from Catholic University of Chile (PUC), Santiago, Chile in 2010. He received his M.Sc, from Politecnico di Milano, Milan, Italy in 2013 and wrote M.Sc. thesis in the TUM, Munich, Germany. He joined MATIS Deutschland GmbH and worked for BMW in the development of power electronics and drives for electric vehicle prototypes. Since 2015 he has been with the Department of Electrical Engineering, PUC Chile as Instructor Professor. In 2015 he founded RT Electronics SpA, where he is currently Chief Technical Officer. His research interests include power electronics, electrical machines and drives, energy storage and electric vehicles. Mr. Repenning was awarded the ASP diploma for his collaboration in aerospace engineering research in Italy 2013.

Jon C. Clare (M'90-SM'04) was born in Bristol, U.K., in 1957. He received the B.Sc. and Ph.D. degrees in electrical engineering from the University of Bristol, Bristol. From 1984 to 1990, he was a Research Assistant and Lecturer with the University of Bristol, where he was involved in teaching and research on power electronic systems. Since 1990, he has been with the Power Electronics, Machines and Control Group, The University of Nottingham, Nottingham, U.K., where he is currently a Professor of power electronics. His research interests include power-electronic converters and modulation strategies, variable-speed-drive systems, and electromagnetic compatibility.

Matias Diaz (S'15) was born in Santiago, Chile. He received the B.S. and the M.Sc. degrees from the University of Santiago of Chile in 2011. Currently, he is pursuing the Ph.D. degree at the University of Nottingham, U.K., and at the University of Chile, Chile. From 2013 to 2015 he was sub-director of the School of Engineering at Duoc UC. Currently, he is a Lecturer at the University of Santiago of Chile. His main research interests include the control of Wind Energy Conversion Systems, Multilevel Converters, and renewable energy systems.